CHAPTER 5

Investigationsfor Efficient Design of a New Counter Flow Double-pass Curved Solar Air Heater

The aim of this chapter is to numerically investigate a new curved design of a counter flow double-pass solar air heater with arched baffles placed in the second duct. Due to high inertia of the flow and curved nature of the design, fluid in the second channel tend to move away from the absorber plate and thus, reduces the thermal efficiency significantly. In order to overcome this deficiency, new design parameter is introduced in the second duct in terms of arched baffles and their design is optimized for various geometric parameters such as angle of attack, variable pitch ratio etc. for best thermo-hydraulic performance. It was observed that arched baffles accelerate the flow near the absorber and facilitate the formation of large secondary vortices that enables multiple attachment zones at the absorber plate. Enhancement in thermal and hydraulic performances are discussed in terms of flow visualization, local Nusselt number, thermal effectiveness and friction factor ratio.The maximum enhancement of Nu in roughened curve counter double pass solar air heater with baffle angles $\alpha/90 = 0.5$ at $P/d = 6$ are found in the range of 20-28%, higher than without baffles. Moreover,Two new regression correlations are developed for prediction of thermo-hydraulic performance in terms of geometrical and flow parameters.

5.1 Introduction

Energy requirement in our daily life has been growing day by day. Solar energy is available in abundance, and it can mitigate the rising energy needs caused by an imbalance between supply and demand. Besides, it is easy to harvest, long-lasting, environmental-friendly, free and an

endogenous energy source. Therefore, solar energy is considered the most promising renewable energy source [8].

A solar air heater (SAH) is a versatile solar thermal device that transforms solar energy into thermal energy. The heated air is used for drying industrial and agricultural product, space heating and many other applications. However, owing to its low thermal efficiency, SAH is not a common commercial device. A SAH device consists of a transparent top glass that allows solar radiation to pass and heat a blackened absorber plate below it. The heated plate, in turn, heats the adjoining air. Depending on the driving force (forced or buoyancy-driven), the heated air is directed through an insulated duct for the desired purpose. From the previous investigations, it has been found that when the heated air is allowed to pass through a double-pass duct rather than a single-pass duct, efficiency improves. Further, it has also been reported that in double-pass ducts, efficiency is higher (nearly 20%) when air flows over the absorber plate in a counter or return type duct design compared to parallel flow ducts[26]. Low convective heat transfer coefficient, i.e. low heat transfer rate between air and absorber surface in parallel flow duct, leads to the higher temperature of the absorber plate, and this manifests into higher radiation losses to the environment[42]. A schematic diagram of a curve counter flow double pass SAH has been shown in Fig.5.1, where fluid returns after being heated first in the upper duct. Apart from absorber and glass, optical and physical properties, the higher heat transfer coefficient or efficiency of such device is strongly dependent on the duct design. This is the reason that previous investigators have focused mainly on the design part of the SAH device.

In the scientific endeavor to improve the heat transfer rate from the heated absorber plate, various innovative design concepts of the duct have been investigated previously. The most prominent method has been to add ribs or turbulators [7, 35, 40, 69, 70, 145] and fin [10, 46] on the absorber plate to break the thin boundary layer. In other words, the heated fluid near the plate should interact with the cold fluid above it to enhance the overall heat transfer rate. For example, Abdullah et at.[2] performed an experimental study using aluminium cans as turbulators on both sides of the absorber in an aligned and staggered arrangement. They reported the maximum efficiency of staggering counter-flow at 68% for the mass flow rate of 0.5 kg/s. Experimental work was carried out by Ravi and Saini [114]to investigate the performance of a double-pass counter flow duct with discrete multiple V-shaped and staggered rib on both surfaces of the absorber plate. The study showed maximum augmentation in Nusselt number more than four times compared to the corresponding smooth counter flow design. Gabhane and Patil [32] performed an experiment to investigate the thermal and hydraulic characteristics of parallel double-pass duct using multiple C-shape ribs as a roughness element. A comparative study has been conducted by El-Sebaii et al.[30] on double pass- V-corrugated and finned plate SAHs. The study reported that double pass-finned plate SAH is about 12% lesser efficient than V-corrugated plate SAH. Ho et al.[46] reported a theoretical and experimental investigation of baffled counter double-pass duct with external recycle and attached internal fins. The study

revealed that baffles created more turbulence and increased heat transfer area, and reduced the boundary layer growth. Ramani et al.[112] presented a theoretical and experimental study of counter double-pass SAH with and without porous material. The porous material was placed in the lower channel. The study reported that the thermal efficiency of double-pass SAH with porous absorbing material was 20 – 25% higher than without porous absorbing material.

Kumar et al.[74] reported some ideas to improve a parallel flow double-pass SAH (DPSAH). They showed that if the parallel duct design is made curved with strategically attached semi-circular ribs on the absorber plate, thermal performance can be enhanced significantly due to the generation of secondary flow vortex near the absorber plate. Recently, Kumar et al.[76] transformed airflow arrangement from parallel design into smooth and roughened counter flow designs of curved DPSAH. They investigated the performance of both the configurations by numerical modelling and found that counter design has 37% more thermal performance than parallel design. Moreover, unequal heat transfer was observed in upper and lower duct with upper duct showing higher heat transfer activities compared to lower duct. The thermal performance in the lower channel suffers due to the nature of flow dynamics, even though it seems counter intuitive (see in Fig.5.1).As fluid comes from the upper to lower channel due to sudden change in flow direction, flow inertia takes the fluid away from the central absorber plate. Further, due to curved nature of the design, heat transfer further reduces in the lower duct[76, 87, 122, 125]. To alleviate the low heat transfer from absorber plate to the fluid in lower channel, suitable design changes would require that would facilitates the incoming fluid to impinge on the heated absorber plate. To the best of the author's knowledge, no such investigations are available in the scientific literature on counter-flow DPSAH alleviated the demerits mentioned above. The main objective of this paper is divided into three parts. (1) to investigate the flow and thermal behaviour of fluid in the lower channel, (2) to optimize the design parameters of lower duct deflectors (see Fig. 5.1), including their shape, size, orientation etc., that would allow the returning fluid to interact (or impinge) on the absorber plate, and (3) to develop new regression correlations for Nusselt number (Nu) and friction factors (f) as a function of flow parameter, i.e. Reynolds numbers (Re) and design parameters. The new correlations would help scientific community in predicting thermo-hydraulic performance of such solar air heaters for a large range of design and flow parameters.

5.2 Problem description and numerical methodology

An unsteady, two dimensional and incompressible flow numerical model is developed of the design shown in Fig.5.1using in ANSYS-FLUENT commercial software. The SIMPLE algorithm and finite volume method (FVM) are employed for coupling pressure-velocity and solving the governing equations. Details of the geometry of the computational domain, grid generation,

boundary condition, governing equation and data reduction are explained in the following subsections.

5.2.1 *Geometry of computational domain*

The computational domain of curved counter DPSAH (henceforth CDPSAH) with arched baffles and CDPSAH without arched baffle (i.e., $P/d = 0$) is depicted in Fig 5.1 (a) and (b), respectively. Both of the geometries have same geometrical parameters and they consist transparent glass sheet, absorber plate with unsymmetrically equipped metallic semicircular ribs and insulating plate. Solar radiation falls on the absorber surface through the transplant glass sheet. The working fluid enters through the inlet in the upper duct (between transparent sheet and absorber plate) and exists from the lower duct outlet (between the insulating plate and the absorber plate). During the flow-through channels, fluid extracts heat from the absorber plate. In roughened curved CDPSAH with baffle, repeated arched baffles are placed on the insulating plate of the lower channel. The various geometrical parameters for the computational domain such as radius of curvature(R), best curvature angle (β)[125], relative roughness pitch (P'/d), relative roughness height (d/H), relative arched baffle pitch (P/d) and relative arched baffle inclination angle ($\alpha/90$) and various operating parameters are enlisted in Table 5.1. In the present investigation, the relative baffle pitch and relative baffle inclination angle are systematically varied and variations in thermal and hydraulic performance are observed.Only backwards-curved baffles are selected. The function of baffles should be to direct all the flows towards the absorber plate and allow flows to move in a downstream direction. If forward arched baffles are used instead of backward arched baffles, it may increase the thermal performance, but it would come at the expense of significant hydraulic losses. This, in turn, would increase the pumping power requirements and hence, higher electricity consumption. On the other hand, straight inclined baffles would do the job of directing the flow towards the plate, however, it won't facilitate the fluid's forward motion in a downstream direction. Hence, backward arched baffles are the best choice between performance and efficiency [94]. This is akin to selecting backwards curved blades in a centrifugal fan over forward or straight blades from the efficiency point of view [127]. Further, design of Fig. 5.1(b) with semicircular ribs is chosen as the base design as this design was observed to exhibit optimum performance in parallel flow DPSAH [74].

5.2.2 *Governing equation and data reduction*

The governing equations of the problem are[108, 123]:

Continuity equation:

$$\frac{\partial \rho}{\partial t} + \nabla.(\rho V) = 0 \tag{5.1}$$

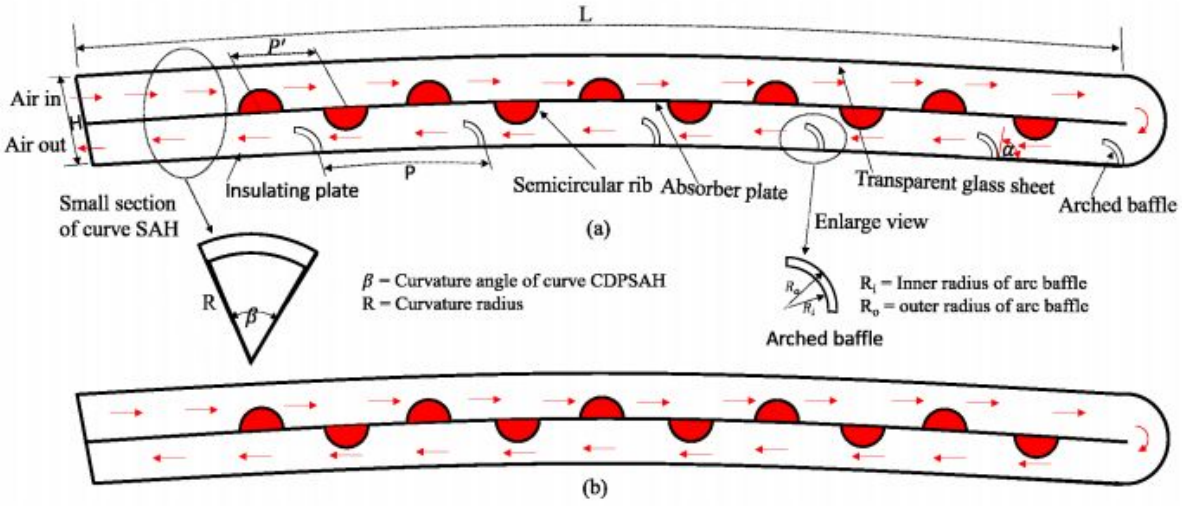

Figure 5.1: Schematic diagram of longitudinal cross section of a double-pass counter flow SAH. (a) Note the strategic placement of arched deflectors in lower channel that directs the fluid towards absorber plate. In second row, left figure show the geometric parameters of the curved SAH. The right figure shows the geometric parameters of the curved baffles, (b) roughened counter DPSAH (i.e., $P/d = 0$) without baffles. Computational model is developed for both the system

Table 5.1: The operating and geometrical parameters considered for the numerical analysis:

Parameter	Value
Reynolds number (Re)	5000, 6000, 7000, 8000, 9000, 10000
Solar radiation (I)	800 W/m^2
Rib diameter (d)	10 mm
Relative baffle pitch (P/d)	4, 6, 8, 10
Relative baffle inclination angle ($\alpha/90$)	0.33, 0.50, 0.67, 0.83, 1.00
Aspect ratio of duct (W/H)	50 (For each lower and upper section)
Relative roughness pitch (P'/H)	0.75
Length of absorber (L)	1600 mm
Duct height (H)	40 mm
Curvature angle of collector (β)	25°
Radius of curvature of collector (R)	3647 mm
Inner radius of arc baffle (R_i)	5.5 mm
Outer radius of arc baffle (R_o)	6 mm
Relative roughness height (d/H)	0.25

Momentum equation:

In x-direction

$$\frac{\partial(\rho u)}{\partial t}+\nabla.(\rho uV) = -\frac{\partial p}{\partial x}+\mu\nabla(\nabla.u)-\nabla\left(\overline{u'V'}\right)+\rho g_x \tag{5.2}$$

In y-direction

$$\frac{\partial(\rho v)}{\partial t}+\nabla.(\rho vV) = -\frac{\partial p}{\partial y}+\mu\nabla(\nabla.v)-\nabla\left(\overline{v'V'}\right)+\rho g_y \tag{5.3}$$

Transport equation for the realizable k-epsilon $(k-\varepsilon)$ model:

$$\frac{\partial(\rho K)}{\partial t}+\nabla.(\rho KV) = \nabla.\nabla(K(\mu+\frac{\mu_t}{\sigma_k}))+G_K+G_b \tag{5.4}$$

$$\frac{\partial(\rho\varepsilon_t)}{\partial t}+\nabla.(\rho\varepsilon_t V) = \nabla.\nabla(\varepsilon_t(\mu+\frac{\mu_t}{\sigma_{\varepsilon_t}}))-\rho C_{2\varepsilon}\frac{\varepsilon_t^2}{K+\sqrt{v\varepsilon_t}}-C_{1\varepsilon}\frac{\varepsilon_t}{K}C_{3\varepsilon_t}G_b \tag{5.5}$$

Energy equation:

$$\frac{\partial(\rho T)}{\partial t}+\nabla.(\rho VT) = \nabla.\nabla((\Gamma+\Gamma_t)T) \tag{5.6}$$

Discrete ordinate radiation model[11, 91]:

$$\nabla.\left(I\left(\vec{r},\vec{s}\right)\vec{s}\right)+(a+\sigma_s)I\left(\vec{r},\vec{s}\right) = an_r^2\frac{\sigma T^4}{\pi}+\frac{\sigma_s}{4\pi}\int_0^{4\pi}I\left(\vec{r},\vec{s}\right)\varphi\left(\vec{s},\vec{S'}\right)d\omega \tag{5.7}$$

Where absorption coefficient (a), scattering coefficient (σ_s),refractive index (n) and phase function (φ) are assume independent of wavelength.

The prediction of fluid flow behavior inside the curve channel is decide by dimensionless parameters Dean number and Reynolds number which are defined as[48]

$$Re = \frac{Inertiaforce}{Viscousforce}=\frac{(\rho UD_h)}{\mu} \tag{5.8}$$

and

$$D_n = Re\sqrt{\frac{D_h}{2R_c}} \tag{5.9}$$

In the present study, the flow is turbulent as the range of Re and D_n are 5000 – 10000 and 497–994 respectively[74, 123].

The convective heat transfer coefficient between air and absorber surface is calculated by applying the energy conservation principle as

$$Q_u = \dot{m}C_{pa}(T_o - T_i) = hA_{eff}(T_p - T_m) \tag{5.10}$$

Where T_m is the bulk temperature of working fluid i.e., $(T_o + T_i)/2$

Thermal performance of SAH represent in term of average Nusselt number (Nu) and thermal effectiveness (ε) which are defined as

$$Nu = \frac{hD_h}{k} \tag{5.11}$$

and

$$\varepsilon = \left(\frac{T_0 - T_i}{T_p - T_i}\right) \tag{5.12}$$

The heat loss from the outer surface of glass cover occurs through convection and radiation heat transfer phenomena, and its combined convection and radiation coefficient is given as

$$h_{(conv+rad)} = \frac{h_{conv}\left(T_g - T_a\right) + \sigma\epsilon\left(T_g^4 - T_{sky}^4\right)}{\left(T_g - T_a\right)} \tag{5.13}$$

The hydraulic diameter of SAH is defined as

$$D_h = \frac{4A_{cross}}{P} \tag{5.14}$$

After evaluating the pressure drop across the duct of SAHs by CFD software their hydraulic performance can be expressed in term of friction factor(f) and calculated by Darcy-Weisbach equation,

$$f = \frac{\Delta P D_h}{2\rho L U^2} \tag{5.15}$$

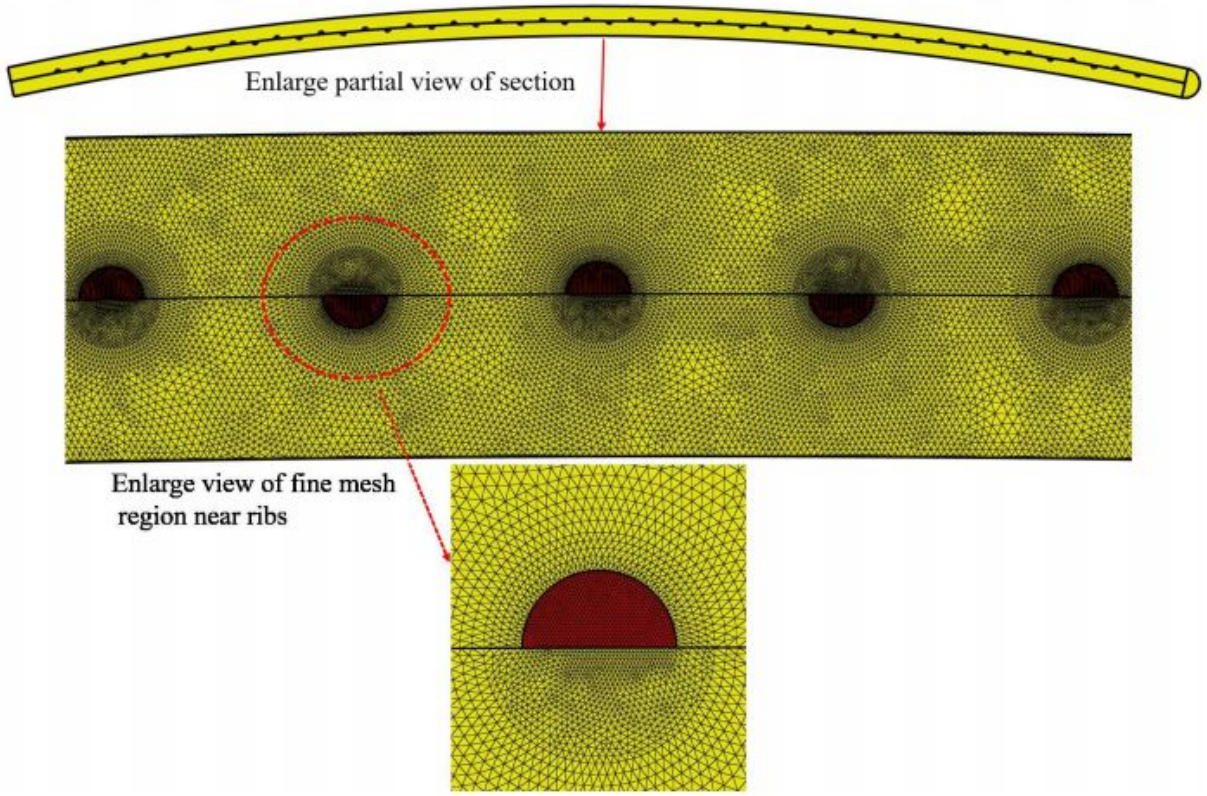

Figure 5.2: Generated mesh on roughened curve CDPSAH

5.2.3 *Grid generation and boundary condition*

5.2.3.1 Grid generation

A very fine mesh is generated near the rib and absorber surface to capture the thermal and hydrodynamic boundary layer gradient (Fig. 5.2). The purpose of the coarse and fine mesh at different locations of the computational domain is to optimize the computational accuracy and CPU time. To report the results that are grid and time step independent, an extensive grid independence and time independence study was done. The interested reader can refer to our previous paper [74]. The same model has been used here for the computational domain shown in Fig.5.1.

5.2.3.2 Boundary and initial conditions

Figure 5.3 shows the description of boundary conditions of the present numerical simulation. Initially, the air inside the computational domain is stagnant at atmospheric pressure with a temperature equal to ambient temperature ($300\,K$). At the inlet, air passes with the uniform velocity at ambient condition ($300K, Pr = 0.7$). The average velocity of air is calculated with respect to the Reynolds number. Air exit from the outlet at atmospheric pressure. A constant solar flux ($I = 800W/m^2$) is applied at the absorber plate (absorptivity of 0.9), while side and

Table 5.2: Properties of materials for numerical simulation [6, 74].

Properties	Symbol	Air	Absorber (Aluminum)	Glass
Density, (kg/m^3)	ρ	1.184	2702	2500
Thermal conductivity, (W/m-K)	K	0.026	273	1.2
Specific heat, (J/kg-K)	Cp	1003	903	800
Dynamic viscosity ,(N.s/m^2)	μ	1.855E-5	-	-
Emissivity	ε	-	0.9	0.88
Refractive index	n	-	1	1.53

arched baffles walls are assumed adiabatic. No-slip boundary conditions applied to all the walls, while the transparent glass sheet with an emissivity of 0.88 is considered to exchange heat with the environment by combined radiation and convection. The wind convective heat transfer coefficient and sky temperature were applied a[10, 28]:

$$h = 2.8 + 3.0V_{\infty} \tag{5.16}$$

and

$$T_{sky} = 0.0552\,(T_a)^{1.5} \tag{5.17}$$

In present numerical modelling, the air is considered as ideal gas. Consequently, the density of air can be expressed as a function of temperature and pressure by using ideal gas law while, other thermo-physical properties such as thermal conductivity (k), specific heat (C_p), dynamic viscosity (μ) are kept constant. Since SAH operated at a low-temperature range and in this range, change in the values of Prandtl number of air is insignificant. This can be justified as the value of Prandtl number at temperature 300 K and 450 K are 0.713 and 0.684, respectively, and it has only a variation of 4% in this range of temperature. Even if variable properties of air are used, outcomes are not expected to change significantly. The thermos-physical properties of working fluid (air) at the inlet section of SAH (at the ambient temperature of 300 K), absorber plate and glass have been listed in Table 5.2.

5.3 Validation of numerical model

In addition to grid generation and boundary condition, another crucial task in the current research consists verifying the accuracy of numerical model by comparing the experimental data with numerical results. The validation of the numerical model has been performed by matching results with experimental outcomes of Mahboub et al.[87]. The numerical simulation has been

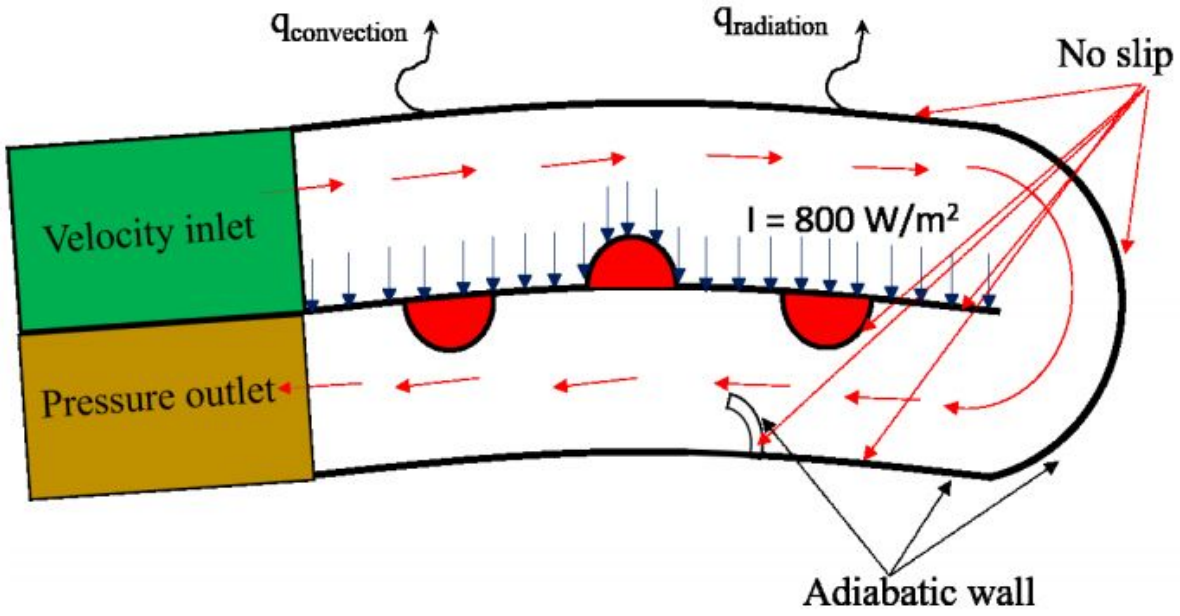

Figure 5.3: Boundary condition used in the numerical simulation

investigated with the same curved geometry as reported in the experimental setup. It was assumed that flow is steady and density of fluid is a function of temperature. A convection boundary condition was applied at the glass cover's top surface to consider combining convection and radiation heat loss through the glass. Mass flow inlet and pressure outlet boundary conditions were assigned at the inlet and outlet of the computational domain. The numerical simulations have been performed for each mass flow rates of 0.0172, 0.029, and 0.0472 kg/sm^2 for the heat flux range $800-1000\ W/m^2$. The Reynolds number evaluated from these mass flow rates comes under the turbulence regime. Therefore, the turbulence model (realizable k-epsilon) was used for turbulence modelling. The difference between the temperature of air at inlet and outlet of the curve SAH were recorded. The variation of temperature difference ($\Delta T = T_0 - T_i$) from numerical and experimental results with solar radiation are plotted in Fig.5.4 for $m = 0.0172$ kg/sm^2. Note that ΔT rises with the increase in solar radiation flux. It has a 9.4% average absolute deviation from experimental outcomes, which comes under an acceptable limit. The percentage deviation in ΔT was calculated as follow:

$$Relative\ error = \frac{(T_0 - T_i)_{numerical} - (T_0 - T_i)_{experimental}}{(T_0 - T_i)_{experimental}} \tag{5.18}$$

5.4 Results and discussion

In this section, results are reported for both: with and without arch baffles while other design parameters remain the same. The effect of position and inclination angle of baffles and Reynolds

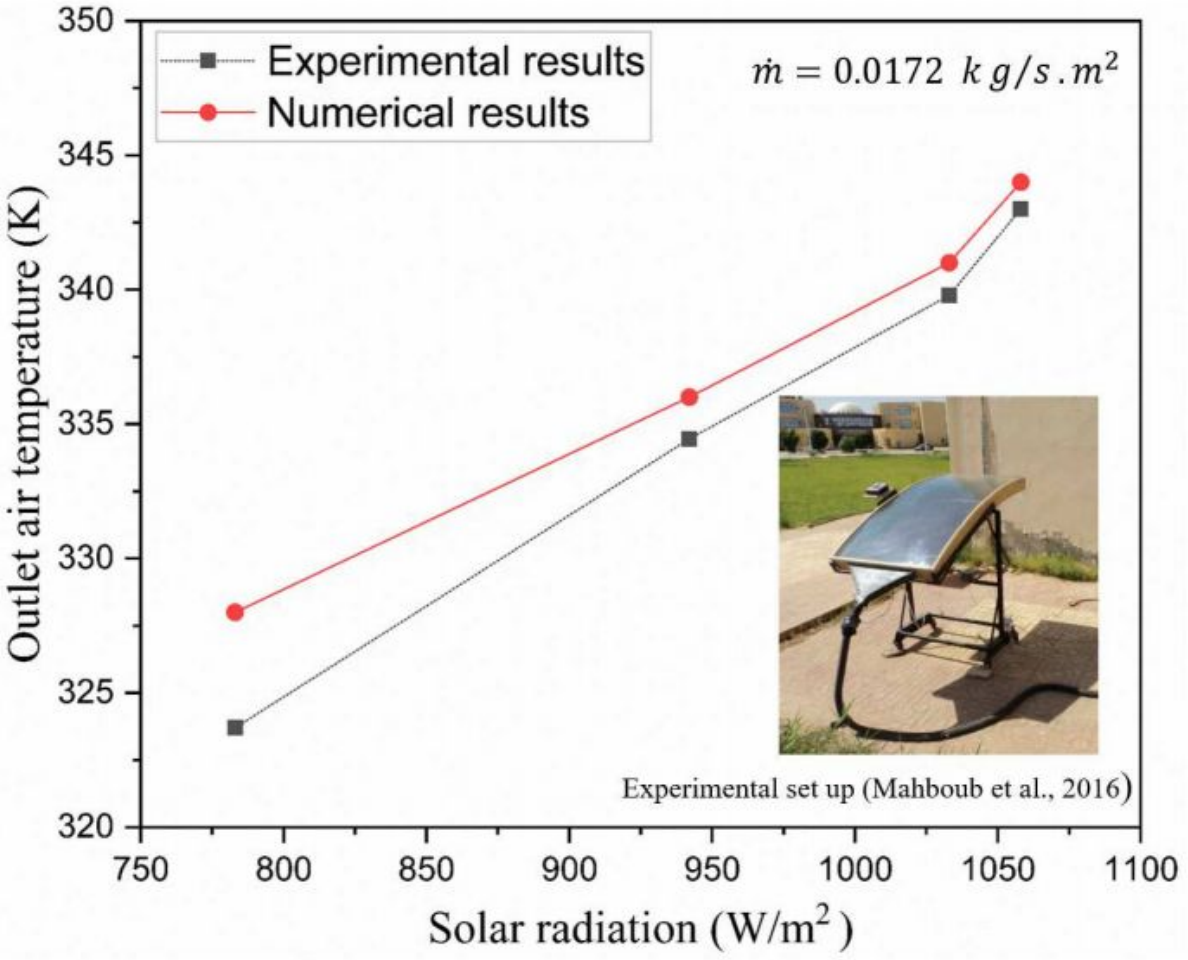

Figure 5.4: Observation of difference between temperature of air at inlet and outlet obtained from CFD and experimental results in a curved SAH. Note that better agreement is observed at higher solar radiation.

number (Re) on the performance are expressed in term of Nusselt number (Nu), thermal effectiveness (ε), local Nusselt number (Nu_x), turbulent kinetic energy (TKE) and friction factor (f).

5.4.1 *Flow visualization*

The effect of arched baffles on the flow field is shown in Fig.5.5 . Flow is from left to right in the upper duct and right to left in the lower duct. Note that two kinds of vortices are formed: primary and secondary vortices. The primary vortices evolved just upstream of the semicircular rib, while secondary vortices are formed downstream of the semicircular rib and between baffles space. Note the following interesting points: (a) All smaller vortices rotate in a clockwise direction except larger secondary vortices. (b) Most of the fluid is directed towards the absorber plate by the arched baffles, creating larger eddies in downstream. (c) The fluid attachment zones with

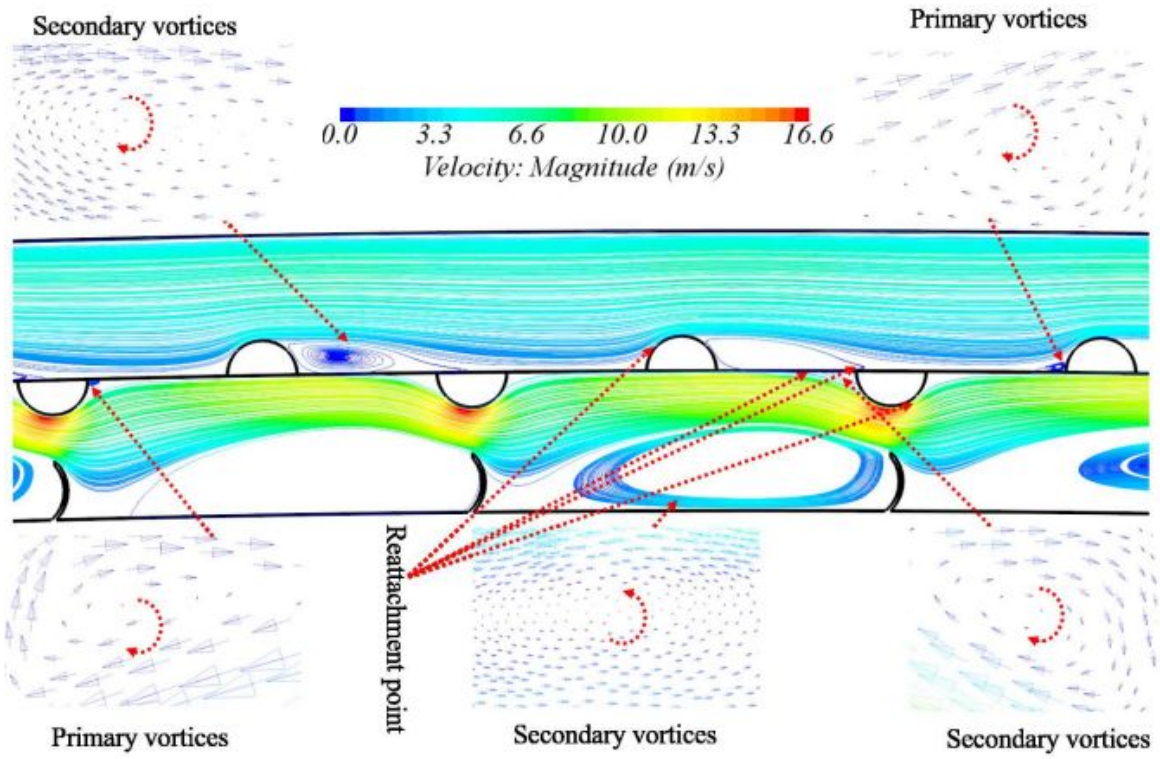

Figure 5.5: Velocity streamline and direction of vortices in curve CDPSAH with baffle ($P/d = 6$ and $\alpha/90 = 0.5$) at fixed Re of 10000.

the absorber plate are initiated before the first semicircular rib in the lower duct due to deflection of flow by arched baffles arrangement and they are comparatively larger. This is expected to increase the heat transfer rates. (d) The nature of vortices is periodic, indicating uniform locations of attachment and separation of fluid with the heated plate and (e) Due to reduced flow area in the lower duct near the absorber plate, flow accelerates near the absorber surface. This acceleration affects the strength of vortices and the heat transfer coefficient between the bottom absorber surface and heated air, which depend on the relative baffle pitch, relative baffle angle, and Reynolds number. It is also seen that baffle position, baffle angle, and Reynolds number significantly impact the size of dominating secondary vortices. All vortices enhance the mixing process of hot and cold fluid, but the mixing rate is higher due to secondary vortices. This is because dominant secondary vortices formed near the high velocity zone (see Fig. 5.5). Consequently, rotating fluid in secondary vortices mix with hot fluid near the absorber surface and increase the convection phenomena. Many researchers have also observed similar phenomena even though their geometrical and operating parameters were different [93].

5.4.2 Optimization of arched baffle pitch

To assess the effect of varying relative arched baffle pitch (P/d) on thermal and hydraulic performance characteristic of SAHs as shown in Fig.5.1, the distance between two array of baffle is increased from $0-100\,mm$ with a step of $20\,mm$ while the size and inclination angle of baffles are kept constant.

Figure 5.6 shows the variation of Nu with P/d in the range of Re of $5000-10000$ for the fixed value of $\alpha/90=1$. It is found that as P/d increases from 0 to 6, the rate of heat transfer enhances significantly; after P/d of 6, the rate of heat transfer declines. This is true for any Reynolds numbers. The enhancement of Nu in CDPSAH with baffle for $P/d=4,6,8$ and 10 at $\alpha/90=1$ are respectively in the range of $7-12\%$, 12-17%, 6-10% and 4-8% higher than without baffles (i.e., $P/d=0$) for the Re range of $5000-10000$.

Figure 5.7 illustrates the variation of thermal effectiveness (ε) with relative baffle pitch (P/d) for the Re range of $5000-10000$ at a constant value of $\alpha/90$ equal to 1. The outcomes revealed maximum ε, i.e., 0.89 for P/d of 6 and at $Re=5000$. As P/d increases from 6 to10 and decreases from 6 to 0, the value of ε decline. This is because as P/d increases from 6 to10 and decreases from 6 to 0, passage area (between the arched baffle and absorber) of flow increases due to shifting of arched baffles and exchange of momentum of fluid with both absorber surface and attached semicircular rib decline. Consequently, turbulent kinetic energy (TKE) increases with escalating P/d from 0 to 6, reaching a maximum at P/d of 6 and then decreases. Clearly, the dynamics of heat transfer change as the relative pitch changes.

To understand the local dynamics of heat transfer, it is necessary to understand the heat transfer locally. We divided a small region into two zones (see Fig5.8): Zone-I is downstream of a baffle while zone-II is just above the baffle containing the semicircular rib. The longitudinal local distribution of the Nusselt number (Nu_x) in the lower channel of CDPSAH with baffles ($P/d=4,6,8,10$ and $\alpha/90=1$) and CDPSAH without baffles ($P/d=0$) at the absorber surface has been depicted in Fig.5.8 for both the zones. In zone-I, the value of Nu_x with baffles has a larger magnitude compared to CDPSAH without baffles. This is due to the presence of baffles that restricts the flow passes area in the lower channel, and the hot fluid lifts upward with larger velocity near the absorber plate and exchanges considerable momentum with the absorber plate. This enhances the heat transfer rate. Consequently, one larger peak in Nu_x appears at the position of impingement (see in Fig. 5.5). Moreover, one small recirculation zone appears near the absorber plate just across the semicircular rib where the fluid is trapped and does not blend with the cold fluid. Thus, the rate of heat loss from the absorber to air decreases. In zone-II the variation of Nu_x along the semicircular ribs' periphery is shown . Just at the start and end of periphery of semicircular ribs, the fluid exchange small momentum with the periphery of semicircular rib and hence, a small recirculation zone, i.e., dead zone is seen (refer Fig. 5.5). Thus, Nu_x values appear minimum. However, just after the first dead zone, fluid comes in

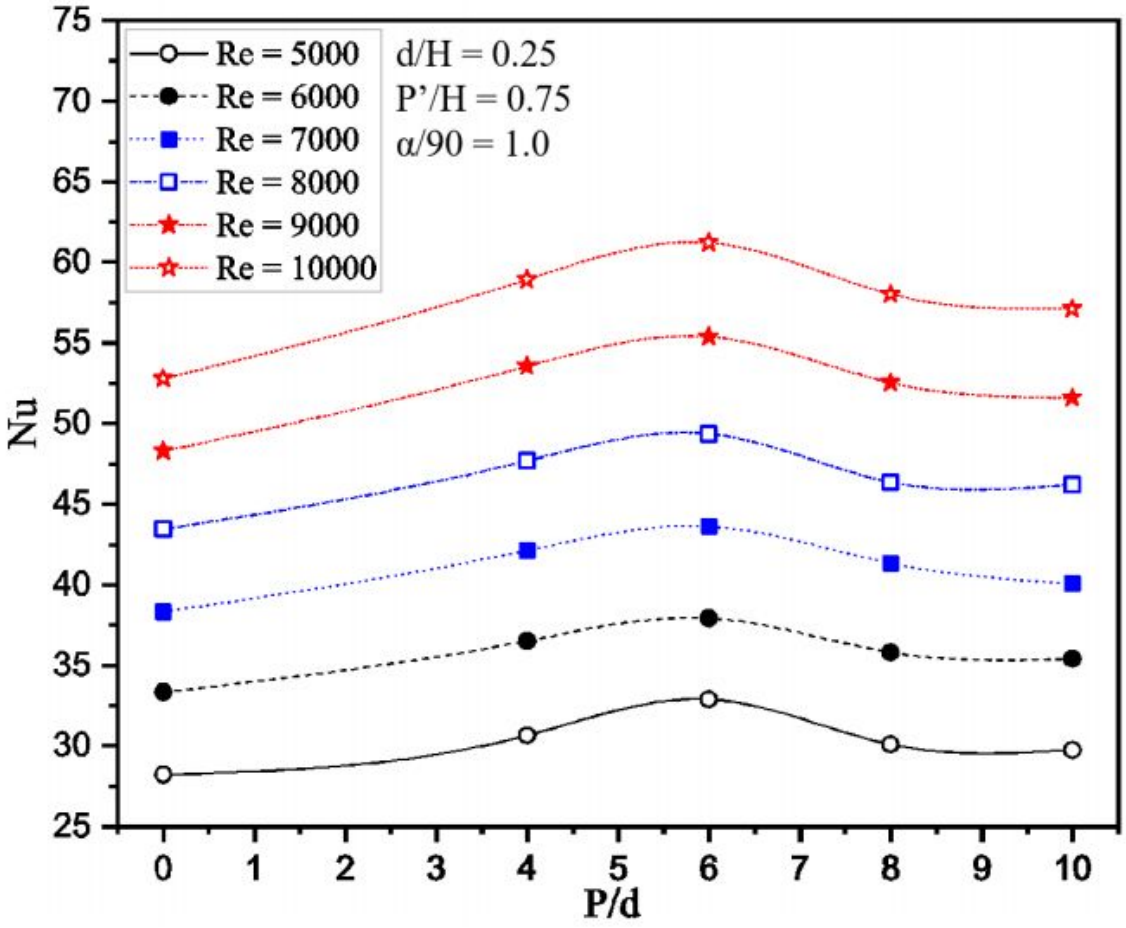

Figure 5.6: A plot of Nu with P/d for different range of Reynolds numbers. Increase and decrease in Nusselt number variation signifies there lies a optimum relative pitch where thermal performance is optimum. Note that lines connecting the values are not a curve fit. It is drawn just to show the trend. This is true for all the figures in this section.

contact with the semicircular rib surface and exchange considerable momentum. This momentum exchange continues to rise till the second dead zone. Consequently, the magnitude of Nu_x variation in CDPSAH with baffles has a larger value than CDPSAH without baffles.

Figure5.9 depicts the variation of friction factor ratio (f_{wb}/f_{wob}) with relative baffle pitch (P/d) of CDPSAH with baffle and without baffle for the range of Re (5000 – 10000) at a constant value of relative baffle angle ($\alpha/90$). As P/d increase from 0 to 6, the friction factor ratio increases significantly. After a P/d of 6, the fiction factor ratio decreases slightly. This is because as P/d increases from 6 to10 and decreases from 6 to 0, passage area (between the arched baffle and absorber) of flow increases due to shifting of arched baffles and obstruction of fluid flow decreases. This obstruction reaches a maximum value at $P/d = 6$ due to the minimum flow passage area. Consequently, maximum value in friction factor ratio has been observed at $P/d = 6$ in the range of Re used. Clearly, hydraulic losses are high where the increase in heat transfer rates are high.

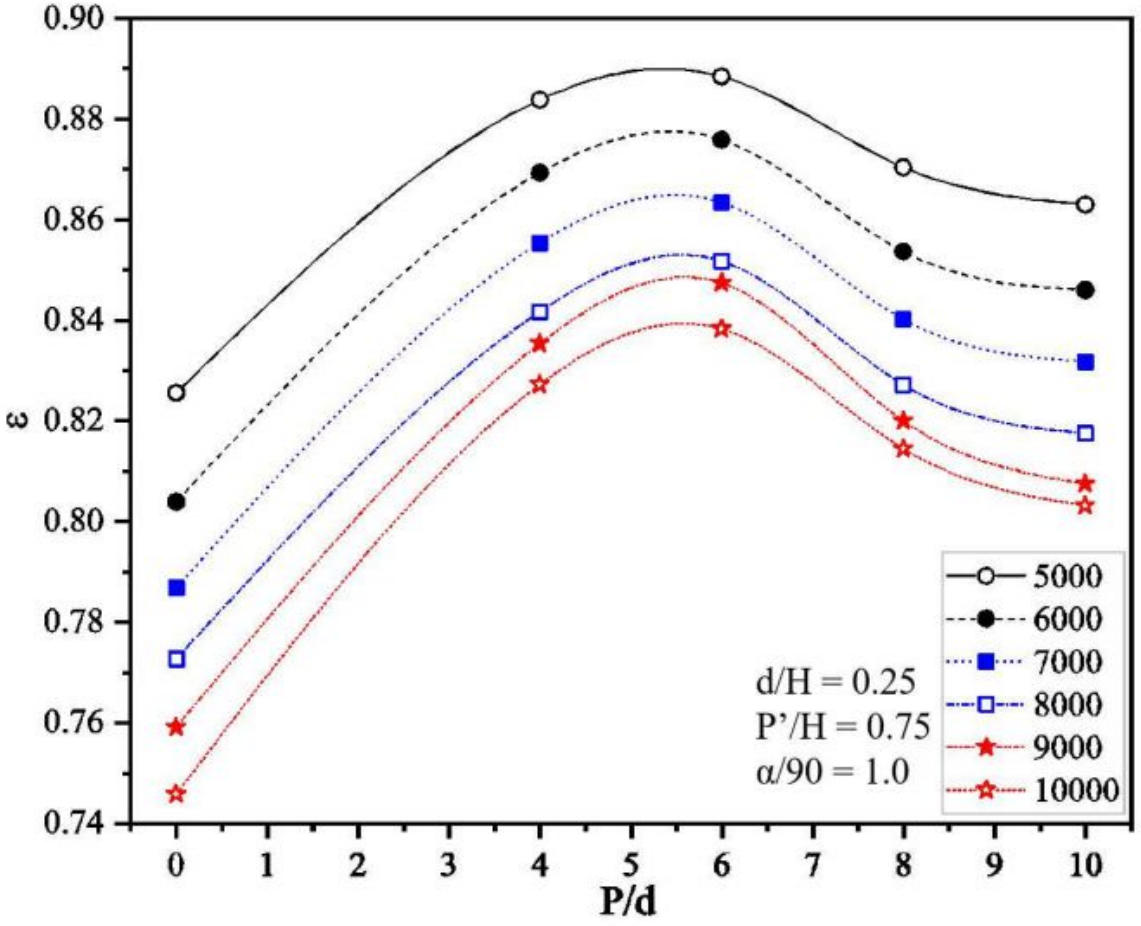

Figure 5.7: The variation of thermal effectiveness (ε) with relative baffle pitch (P/d).

5.4.3 *Optimization of arched baffle angle*

As we observed in the previous section (see Fig. 5.5), fluid attachment zones in a lower section can change if the inclination of the baffle angle change. To assess the influence of varying relative baffle angle on thermal and hydraulic performance characteristic of SAHs, the inclination angle of baffle varied from $30-90$ degree with a step of 15 degrees anticlockwise while size and distance between two arrays of baffles are kept constant. Figure5.10 demonstrates the variation of Nu with $\alpha/90$ in the Re range of $5000-8000$. Nu increases with a rise of $\alpha/90$ and attain peak value at $\alpha/90 = 0.5$, then decreases with an increase in $\alpha/90$. The magnitude of average velocity was observed to be high at $\alpha/90 = 0.5$ and large secondary vortices behind baffles are formed. Consequently, fluid exchanges significant momentum with the absorber plate and hot fluid mix with cold fluid to extract a large amount of heat from the absorber plate. Moreover, a variation of Nu with $\alpha/90$ follow the same trend for all cases of Re. The enhancement of Nu in roughened curve CDPSAH with baffle angles $\alpha/90 = 0.33, 0.5, 0.63, 0.87$ and 1 at $P/d = 6$ are respectively in the range of 14-25%, 20-28%, 12-21% and 9-14% higher than without baffles (i.e., $P/d = 0$).

Since heat transfer augmentation and hydraulic losses are correlated, it is imperative to un-

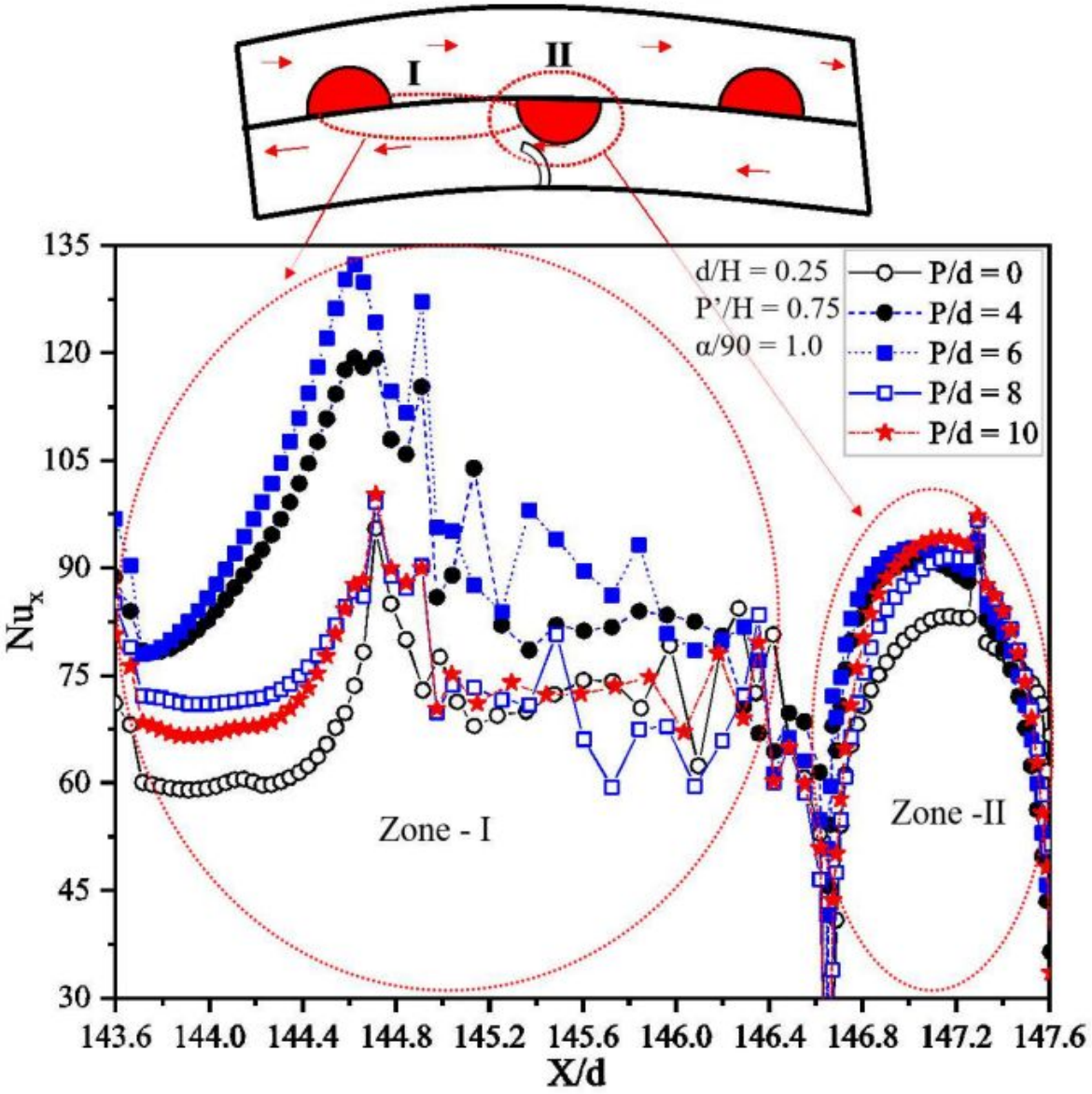

Figure 5.8: variation along the longitudinal length of absorber plate in lower channel of CDP-SAH at Re = 10000

derstand the variation in friction factor with baffle angle. Fig.5.11. illustrates the variation of friction factor ratio (f_{wb}/f_{wob}) with relative baffle angle ($\alpha/90$) for the range of Re 5000 – 10000. The f_{wb}/f_{wob} increases sharply with the rise of $\alpha/90$ from 0.33 to 0.5 and reaches the maximum value at 0.5 then decreases with a rise of $\alpha/90$. Note that $\alpha/90 = 0.5$ corresponds to $\alpha = 45$. Hence, for optimum heat transfer, the arched baffles should be included at about 45 along the flow direction.

To understand and visualize the effect of relative baffle angle ($\alpha/90$) on flow structures, comparisons are shown with and without baffles for various angles. Fig.5.12 shows the turbulent kinetic energy (TKE) fields for a given Re and P/d ratio. It is observed that TKE increases with

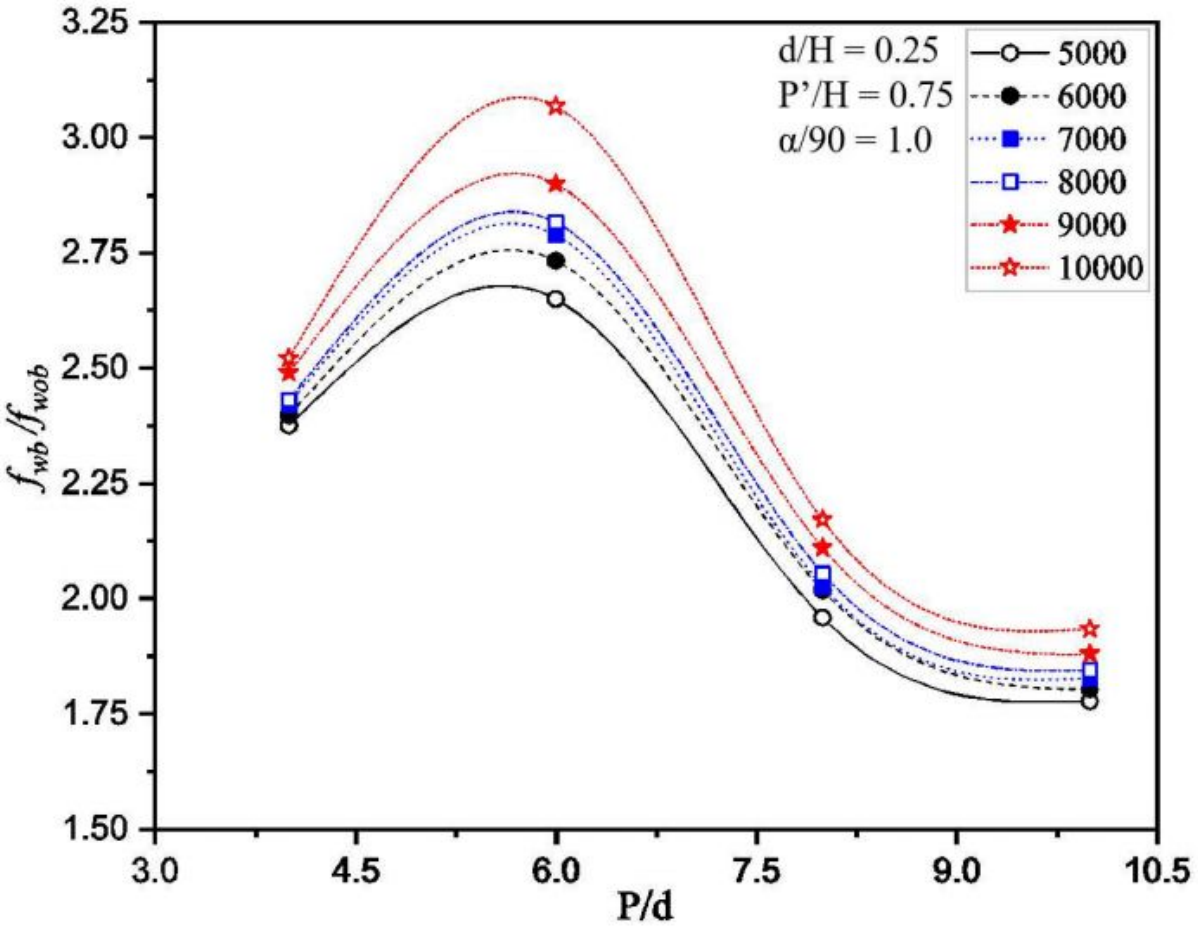

Figure 5.9: Variation of friction factor ratio (f_{wb}/f_{wob}) vs relative baffle pitch (P/d).

the decrease of $\alpha/90$ from 1 to 0.5 and reaches a maximum at $\alpha/90 = 0.5$, and decreases afterwards with further decrease in $\alpha/90$. The sudden contraction and expansion in fluid passes area formed between the absorber plate (i.e., semicircular rib) and upper part of the baffle results in enhanced mixing. Hence, the accelerating flow create large recirculation zones. Consequently, a high TKE zone occurs between the upper part of the baffle and absorber plate (i.e., semicircular rib) and downstream of the baffle. This can also be seen from the graph of Nu vs $\alpha/90$ (Fig. 5.10).

Figure 5.13 depicts the local velocity distribution along with the relative height of the CDP-SAH with baffles for a fixed value of Re and P/d along a longitudinal distance 'aa' situated at 1515 mm length. Flow behavior is investigated into three zones (I, II and III). Zone-I and II belong to the lower channel, while zone-III belongs to the upper channel. Note the average velocity in zone-II (near absorber plate) is highest followed by zone-III and zone-II (below the absorber plate or just downstream of arched baffle). Formation of large secondary vortices are responsible for low velocity near the arched baffles. Flow in Zone-I and II is mixed by both semicircular ribs and baffles, while zone-III fluid is only mixed by semicircular ribs. Due to high velocity in

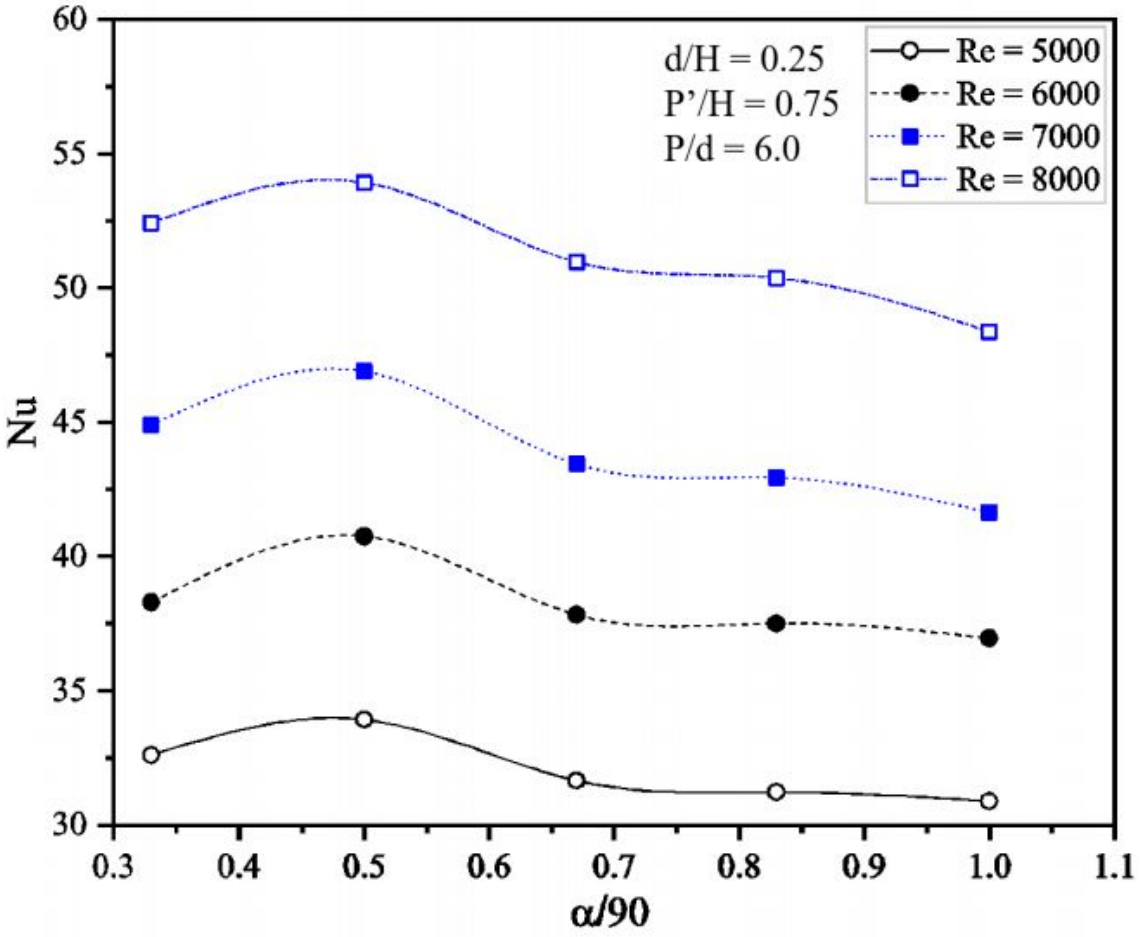

Figure 5.10: Variation of Nu with baffle angle $\alpha/90$.

zone-II, higher heat transfer is expected as observed before. In contrast, zone-III has a maximum velocity at slightly above the absorber plate, partly due to centrifugal forces produced from the duct's curvature and partly due to semi-circular ribs. It is also observed that the order of magnitude of maximum velocity inside the domain (Zone-I, II and III) depends on the passage area design between the baffles and absorber plate. In all three zones maximum velocity occurs at a relative baffle angle $\alpha/90 = 0.5$.

5.5 Regression correlation for roughened curve CDPSAH with baffle

From the results and discussions in previous section, it was observed that Nusselt number and friction factor are strongly influenced by flow parameter (Re) and geometrical parameters of baffles (relative baffle pitch and relative baffle angle). Therefore, the functional relationship of Nu and f are written as:

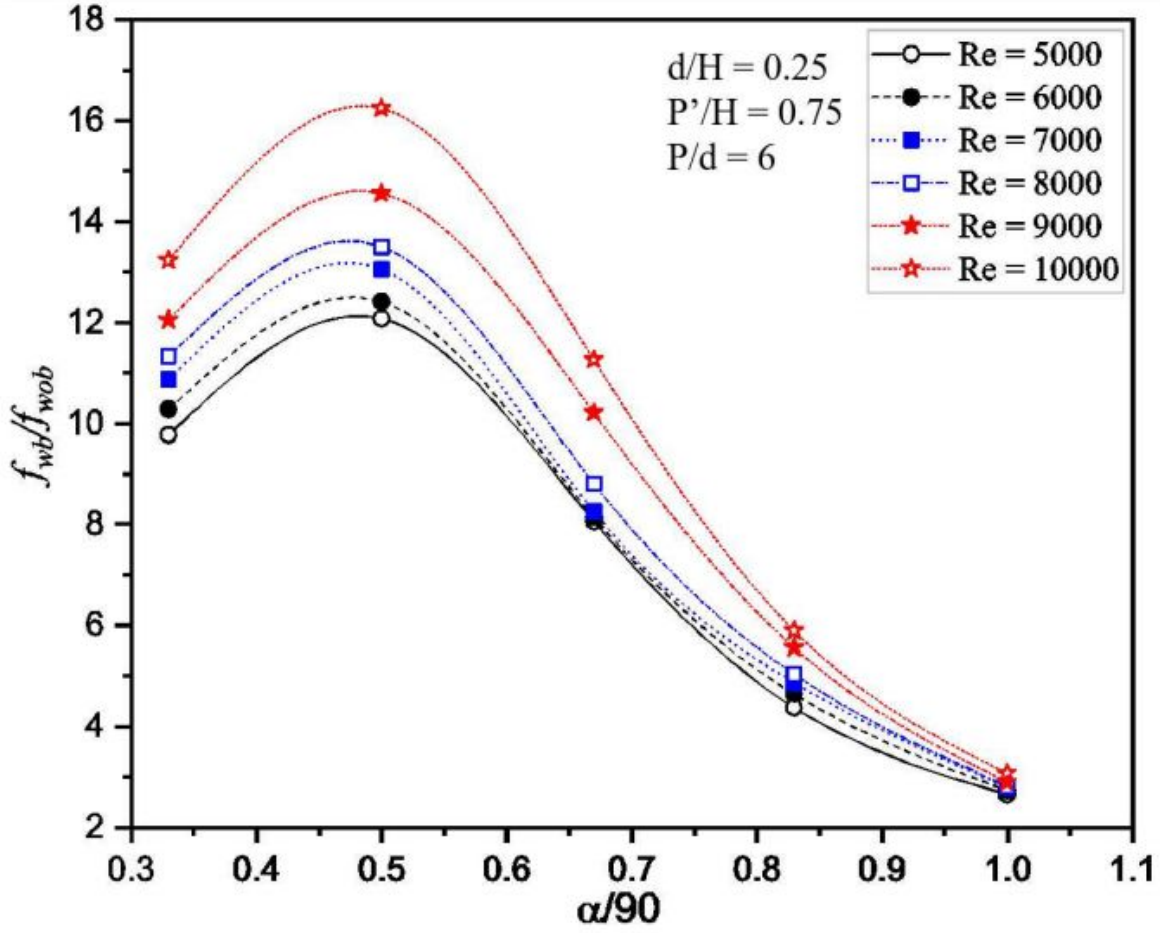

Figure 5.11: Plot of friction factor ratio (f_{wb}/f_{wob}) with relative baffle angle ($\alpha/90$).

$$Nu = f_1\left(Re, \frac{P}{d}, \frac{\alpha}{90}\right) \tag{5.19}$$

$$f = f_2\left(Re, \frac{P}{d}, \frac{\alpha}{90}\right) \tag{5.20}$$

The functional form of function f_1 and f_2 are derived from the regression correlation method as described below using same procedure given by Kumar and Layek [75].

5.5.1 *Regression correlation for Nusselt number*

The set of data points of Nu and Re for distinct values of P/d has been plotted on log-log scale as presented in Fig.5.14. A straight line is used to fit these data point by the method of regression analysis and has the form:

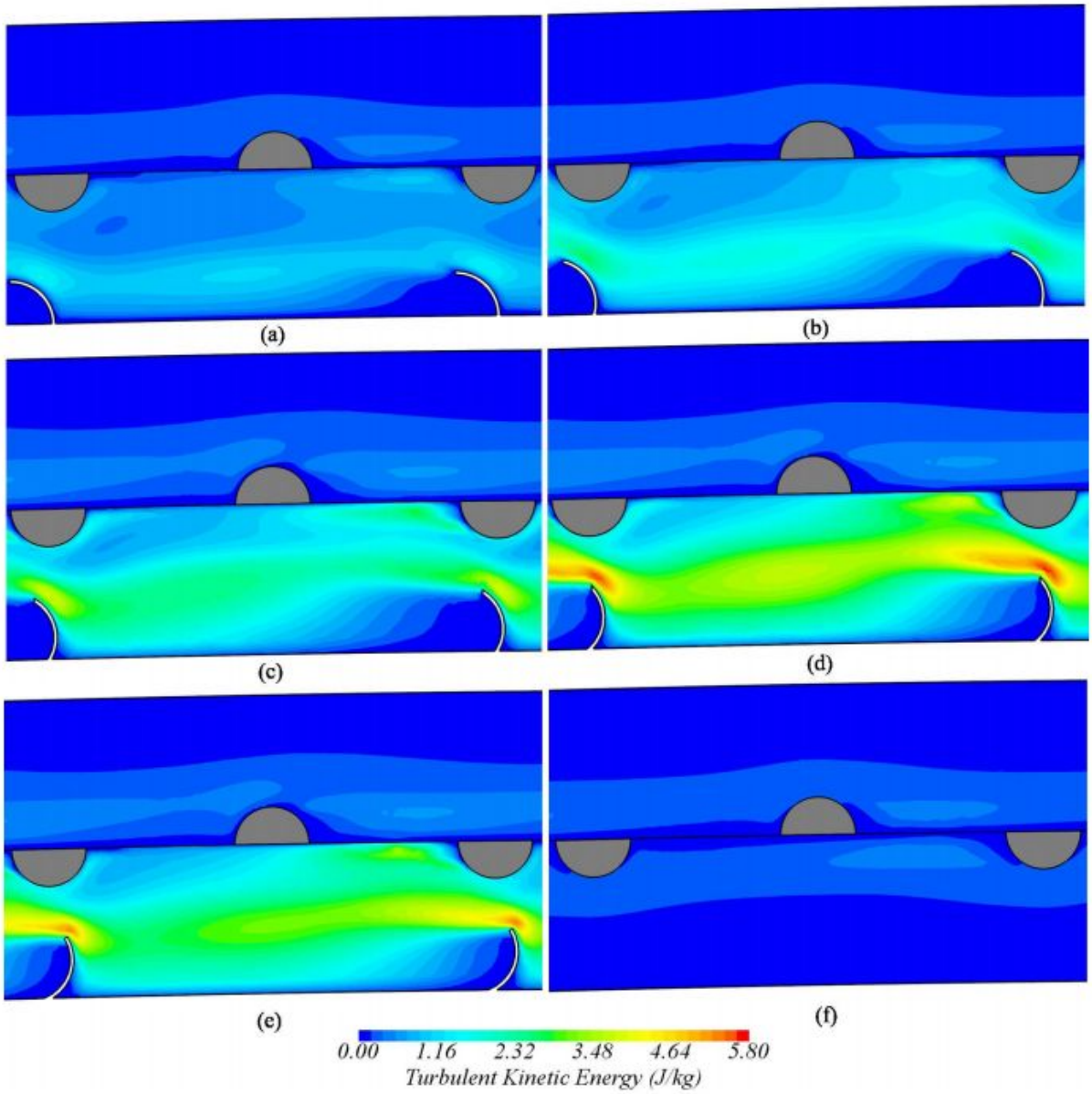

Figure 5.12: Contour plots of turbulent kinetic energy at $Re = 6000$ and $P/d = 6$ for (a) $\alpha/90 = 1$, (b) $\alpha/90 = 0.83$, (c)$\alpha/90 = 0.67$, (d) $\alpha/90 = 0.5$, (e) $\alpha/90 = 0.33$ and (f) for $P/d = 0$ i.e. without baffles.

$$Nu = A_0 Re^{1.0019} \tag{5.21}$$

A_0 in the above equation, depends on another baffle parameter i.e., P/d. All the data points of A_0 are plotted against P/d on log-log scale and a new relation has been derived by using regression analysis. This new relation has been expressed as:

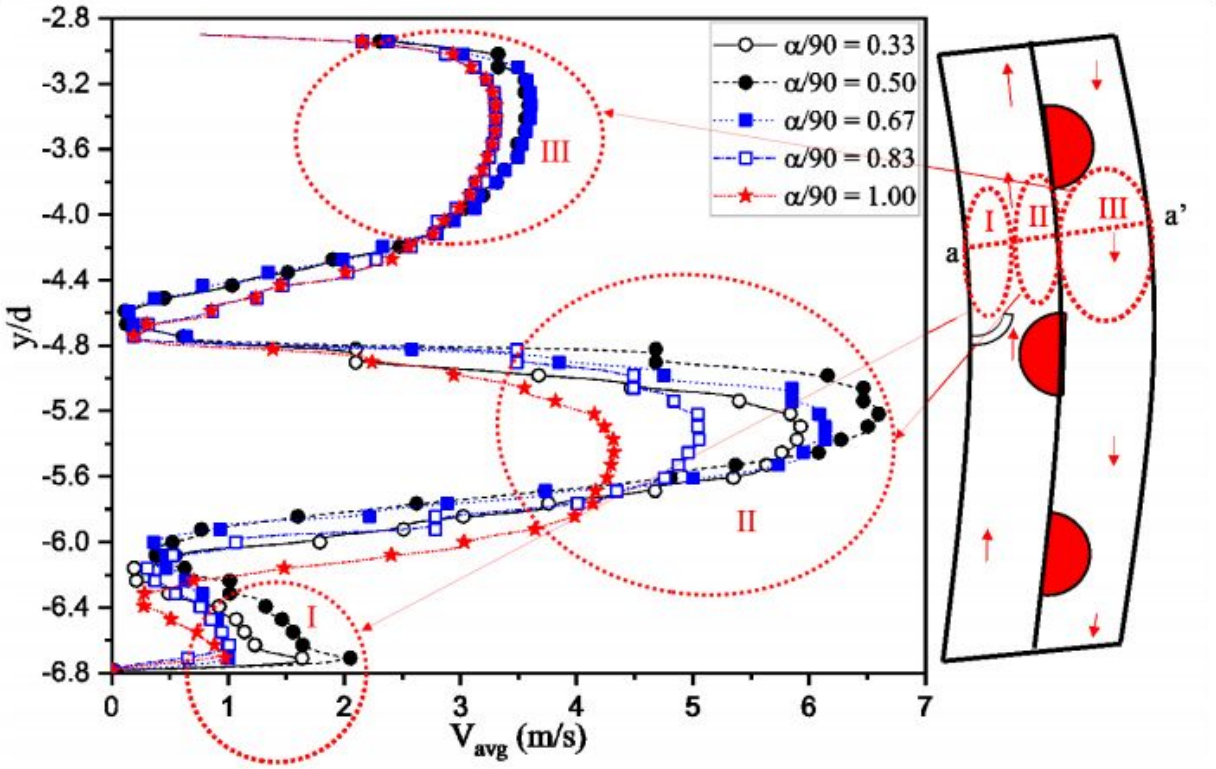

Figure 5.13: Variation of local velocity along the duct height (along aa' line) at a longitudinal distance of 1515 mm at $Re = 6000$ and $P/d = 6$. Zones are marked in the right panel schematic figure.

$$ln\left(\frac{Nu}{Re}\right) = B_2 ln(P/d)^2 + B_1 ln(P/d) + ln(B_0) \tag{5.22}$$

This equation can be written in simplified form as:

$$B_0 = \frac{Nu}{Re^{1.0019}\left(\frac{P}{d}\right)^{0.3009} exp\left[-0.0888\left\{ln\left(\frac{P}{d}\right)\right\}^2\right]} \tag{5.23}$$

where B_0 is the function of $\alpha/90$. A regression method is employed to fit second order polynomial through these data points is given by

$$ln(B_0) = C_2 ln(\alpha/90)^2 + C_1 ln(\alpha/90) + ln(C_0) \tag{5.24}$$

After simplification, the expression of Nu given as:

$$Nu = 0.00463 Re^{1.0019}\left(\frac{P}{d}\right)^{0.3009} exp\left[-0.0888\left\{ln\left(\frac{P}{d}\right)\right\}^2\right]\left(\frac{\alpha}{90}\right)^{-0.1483} exp\left[-0.0689\left\{ln\left(\frac{\alpha}{90}\right)\right\}^2\right]$$

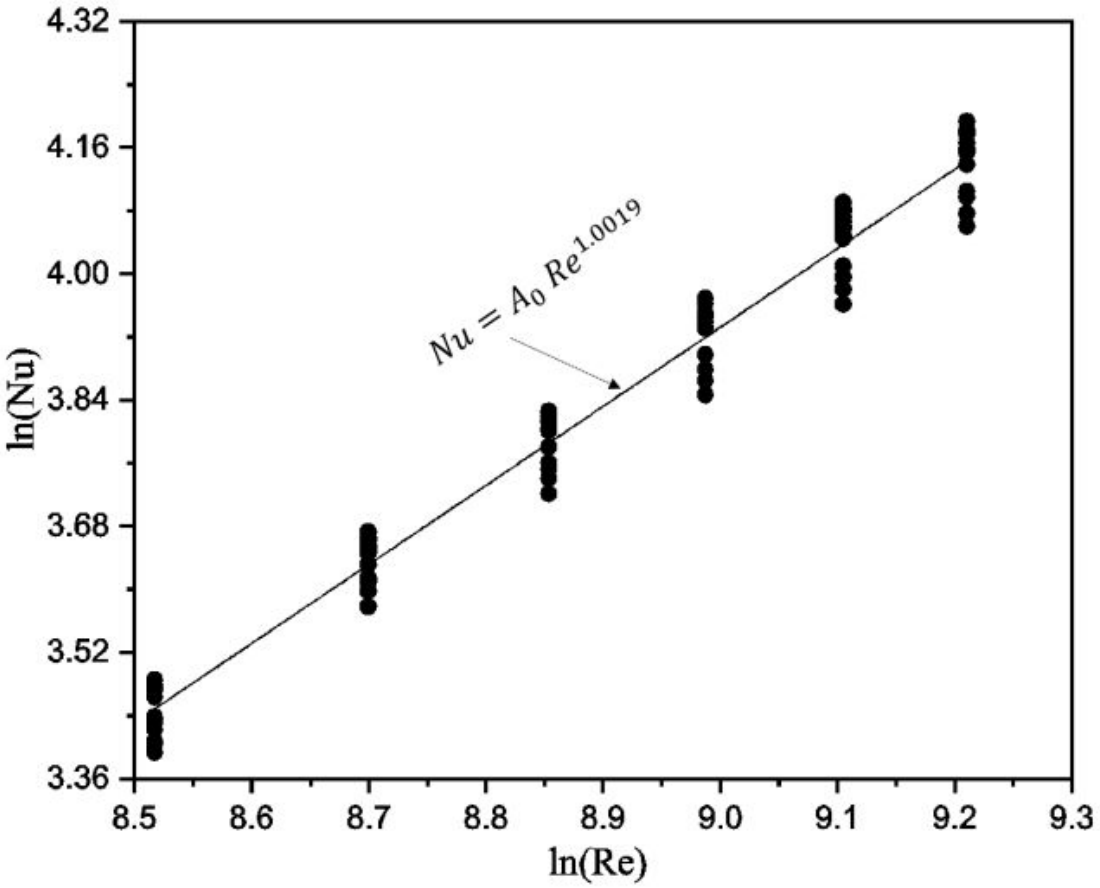

Figure 5.14: Variation of $ln(Nu)$ with $ln(Re)$.

5.5.2 *Regression correlation for friction factor*

The functional relationship of f with Re, P/d and $\alpha/90$ has been established by similar technique as discoursed above.

The final expression of friction factor is expressed as:

$$f = 3.8 * 10^{-7} Re^{0.0272} \left(\frac{P}{d}\right)^{14.142} exp\left[-4.12\left\{ln\left(\frac{P}{d}\right)\right\}^2\right] \left(\frac{\alpha}{90}\right)^{-3.1619} exp\left[-1.8718\left\{ln\left(\frac{\alpha}{90}\right)\right\}^2\right]$$

The comparison of numerical and predictions from the derived correlation of Nu and f are depicted in Fig.5.15 and 5.16 respectively. The deviation or error of ± 1.6% and ± 7.6% is observed between the numerical and predict values of Nu and f . Considering the large range of data used, the deviations are within acceptable limit and hence, the proposed regression correlations can be used with reasonable accuracy to predict the system thermal and hydraulic performance.

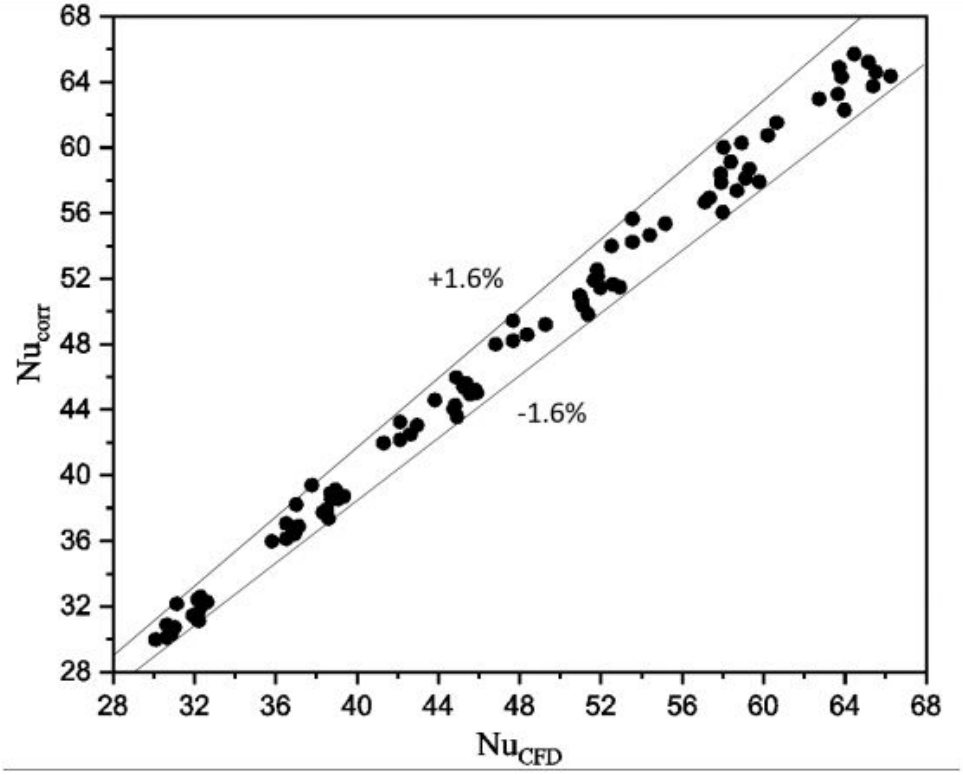

Figure 5.15: Variation of predicted and numerical value of Nu.

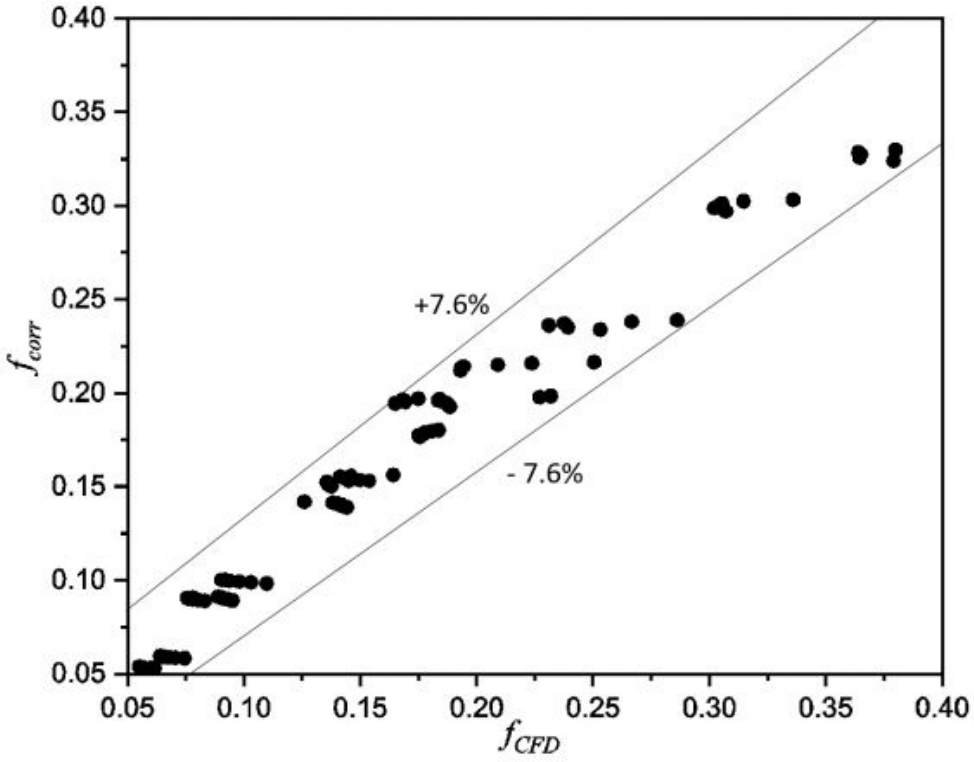

Figure 5.16: Comparison of numerical and forecasted values of friction factor.

5.6 Conclusions

In this chapter, a new curved design of counter flow double-pass solar air heater (CDPSAH) with arched baffles has been investigated numerically. Focus of design optimization was the second duct where thermal performance was observed to be low due to curve nature of the solar air heater. Arch baffles were introduced and its design parameters are optimized for higher thermal performance. Large secondary vortices are observed in the second duct on downstream of the arched baffles. Due to high acceleration and more reattachment zones, higher heat transfer coefficient was observed in the second channel, thereby increasing the overall performance of the system. The maximum thermal and hydraulic performance has been achieved at the configuration at relative pitch ratio $P/d = 6$, relative baffle angle $\alpha/90 = 0.5$.The maximum enhancement ofNu in roughened curve CDPSAH with baffle angles $\alpha/90 = 0.5$ at P/d =6 are found in the range of 20-28%, higher than without baffles. Moreover, two new regression correlations are developed to predict the thermal (in terms of Nusselt number) and hydraulic performance (in terms of friction factor) of the curved DPSAH. The developed formula agrees well the numerical data with an error of ± 1.6% and ± 7.6% in Nu and f respectively. The authors hope that design and data presented in this research would be beneficial to the scientific community in developing further efficient designs to harness solar energy.